A study of defect structures in Fe-alloyed ZnO: Morphology, magnetism, and hyperfine interactions

Valentin N. Ivanovski [iD], Jelena Belošević–Čavor [iD], Vladimir Rajić [iD], Ana Umićević [iD], Smilja Marković [iD], Vladan Kusigerski [iD], Miodrag Mitrić [iD], and Vasil Koteski [iD]

View Online   Export Citation   CrossMark

A study of defect structures in Fe-alloyed ZnO: Morphology, magnetism, and hyperfine interactions

Valentin N. Ivanovski,[1,a)] Jelena Belošević-Čavor,[1] Vladimir Rajić,[1] Ana Umićević,[1] Smilja Marković,[2] Vladan Kusigerski,[1] Miodrag Mitrić,[1] and Vasil Koteski[1]

AFFILIATIONS

[1]Vinča Institute of Nuclear Sciences, University of Belgrade, Belgrade 11001, Serbia
[2]Institute of Technical Sciences of SASA, Knez Mihailova 35/IV, 11000 Belgrade, Serbia

[a)]Author to whom correspondence should be addressed: valiva@vin.bg.ac.rs. **URL:** www.vin.bg.ac.rs/en/science/researchers.

ABSTRACT

In order to study the effect of Fe cation substitution on the local structure, defect formation, and hyperfine interactions in ZnO, Mössbauer spectroscopy measurements of the microwave processed $Zn_{1-x}Fe_xO$ ($x = 0.05$, 0.10, 0.15, and 0.20) nanoparticles, together with *ab initio* calculations, were performed. Complementary information on the distribution of particle size and morphology, as well as magnetic properties, were obtained by X-ray diffraction, transmission electron microscopy, and squid-magnetometry. The selected model for analyzing the Mössbauer spectra of our samples is a distribution of quadrupole splittings. The fitting model with two Lorentz doublets was rejected due to its failure to include larger doublets. The Fe^{3+} ions do not yield magnetic ordering in the samples at room temperature. The results from first-principles calculations confirm that the major component of the Mössbauer spectra corresponds to the Fe-alloyed ZnO with Zn vacancy in the next nearest neighbor environment. The magnetic measurements are consistent with the description of the distribution of iron ions over the randomly formed clusters in the ZnO host lattice. While at room temperature all the samples are paramagnetic, magnetic interactions cause a transition into a cluster spin-glass state at low temperatures.

Published under license by AIP Publishing. https://doi.org/10.1063/1.5095837

I. INTRODUCTION

ZnO has been one of the most investigated oxides in recent years due to its excellent semiconductor properties, wide bandgap, affordability, and nontoxicity.[1–3] Modification of the ZnO properties by impurity incorporation is currently being debated in the context of possible applications in ultraviolet optoelectronics and spin electronics. Among the various doped ZnO materials, ZnO doped with Fe is one of the materials that has attracted much attention, because it could potentially benefit to the practical application of ZnO as an optical component[4] and diluted magnetic semiconductor.[5,6] Xu and Li[4] have reported that 1 at.% Fe incorporation can improve the crystalline quality and enhance the UV emission of ZnO thin film. Several authors have experimentally observed room temperature (RT) ferromagnetism in some Fe-doped ZnO samples, materials in the form of thin films,[5–7] nanoparticles,[8–13] and nanorods.[14,15] Recently, photoenhanced magnetization in

Fe-doped ZnO nanowires deficient in oxygen slightly below room temperature was reported,[16] which could expand application of ZnO to the emerging field of optospintronics. However, despite a lot of research work that has been reported on this system, some issues, like the maximum solubility of iron in the ZnO lattice and the actual oxidation state of iron, still remain unclear. Namely, it was shown from the Mössbauer effect, X-ray absorption fine structure (XAFS), electron spin resonance spectroscopy (ESR), and X-ray photoelectron spectroscopy (XPS) measurements that Fe atoms occupy the host ZnO lattice in two different oxidation states, Fe^{2+} and Fe^{3+},[8–10,12,17–19] but there are also studies in which only Fe^{3+} ions were observed.[11,13–15] These contradictory experimental results are probably associated with different defects or impurities created by different preparation methods. Intrinsic defects, mainly O vacancy (V_O) and Zn vacancy (V_{Zn}), seem to play an important role. In the present work, $Zn_{1-x}Fe_xO$ ($x = 0.05$, 0.10, 0.15, and 0.20) nanostructures were synthesized by a microwave-assisted

technique, which offers many advantages, such as inexpensiveness and short synthesis time. Crystal structure and phase composition of the synthesized samples were checked by powder X-ray diffraction (XRD), while particle size distribution and morphology were determined by transmission electron microscopy (TEM). Comprehensive sets of magnetic measurements were conducted to investigate samples' magnetic properties and their possible correlation with iron concentration. We employed Mössbauer spectroscopy to study the effect of the amount of the iron on the local structure and hyperfine interaction parameters. In addition, using the density functional theory (DFT) based linearized augmented plane waves (LAPW) method, we computed interatomic distances, isomer shift, quadrupole splitting, and hyperfine magnetic field at Fe position in wurtzite Fe-alloyed ZnO. Finally, we calculated the above mentioned quantities in the presence of the intrinsic defects, V_{Zn} and V_O, taking into account the possible charge states of the cell after the defect creation.

II. EXPERIMENTAL DETAILS AND RESULTS

A. Sample synthesis

ZnO powders with nominal compositions $Zn_{0.95}Fe_{0.05}O$, $Zn_{0.90}Fe_{0.10}O$, $Zn_{0.85}Fe_{0.15}O$, and $Zn_{0.80}Fe_{0.20}O$ (nominal cation substitution 5, 10, 15, and 20 at.%, respectively) were prepared by microwave processing of precipitate. Starting chemicals, zinc chloride ($ZnCl_2$, purity >99.5, Lach-Ner, Neratovice, Czech Republic), sodium hydroxide (NaOH, purity 98%, Kemika, Zagreb), and iron (III) chloride hexahydrate ($FeCl_3 \times 6 \times H_2O$, Acros Organics, Geel, Belgium) were used as received from the manufacturers. Appropriate amounts of $ZnCl_2$ and $FeCl_3 \times 6 \times H_2O$ were dissolved in 100 ml of distilled water. Separately, 2.8 g of NaOH were dissolved in 40 ml of distilled water and were added dropwise into the above mentioned solution under constant stirring. After being stirred at 50 °C for 90 min, the as prepared precipitate was processed in a microwave oven (2.45 GHz, 130 W) for 5 min. After cooling to room temperature (RT), suspension was centrifuged at 5000 rpm for 10 min, rinsed at least five times with distilled water and consequently with absolute ethanol to remove the surface residual of the starting chemical solutions, and air dried in an oven at 60 °C for 24 h.

B. X-ray diffraction

The X-ray diffraction measurements recorded at Philips PW-1050 with Cu $K_{\alpha 1,2}$ radiation confirmed the wurtzite hexagonal structure ($P6_3mc$, space group number 186) of all samples. Besides, the ZnO sample alloyed with 20 at.% Fe contains a small amount of $ZnFe_2O_4$ spinel crystal phase. The impurity spinel phase is detected via the barely visible peak at $2\theta = 35.3°$ in the vicinity of the highest wurtzite peak (Fig. 1). Another distinguishable peak of the $ZnFe_2O_4$ from the wurtzite pattern makes convolution with the peak of ZnO at $2\theta = 62°$. The measurements showed that lattice constants and c/a ratio did not change much (about 0.03%) upon doping.

Crystallite size and microstrain were calculated by using the X-ray Line Profile Fitting Program (XFIT) with a Fundamental Parameters convolution approach to generating line profiles.[20]
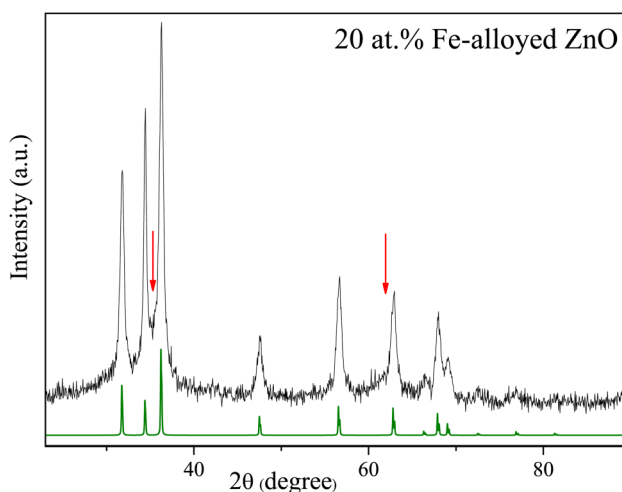

FIG. 1. XRD pattern of 20 at.% Fe-alloyed ZnO with the wurtzite hexagonal structure at RT. The pattern of pure ZnO with $P6_3mc$ space group (olive color) is depicted below the main sample pattern for comparison. The left red arrow denotes the slightly visible peak of $ZnFe_2O_4$ spinel structure at $2\theta = 35.3°$. The right red arrow is pointed toward the convolution peak of wurtzite and spinel structures at $2\theta = 62°$.

Table I shows that the synthesized powders are actually nanostructured, with the average crystallite sizes ranging from 11.5 to 13.8 nm.

C. Transmission electron microscopy

The ZnO nanoparticles were visualized using a FEI Talos F200X transmission electron microscope operating at an accelerating voltage of 200 kV. The samples for TEM examination were prepared by standard procedure where the ZnO powders were first dispersed into ethanol and then a drop of the suspension was placed on a carbon-coated copper grid, which was allowed to air dry. Size distribution of nanoparticles was extracted from the TEM images, and the mean diameters of the particles were measured using the Image J software.[21]

Morphology of Fe-alloyed ZnO nanoparticles was characterized by transmission electron microscopy. The representative TEM

TABLE I. XRD and TEM characterization of the samples. x is the nominal amount of Fe. Crystallite size, microstrain, range of particle size distribution, and $\bar{d}-$ average particle size of the $Zn_{1-x}Fe_xO$ for $x = 0.05$, 0.10, 0.15, and 0.20 are presented.

	XRD		TEM	
x	Crystallite size (nm)	Microstrain (%)	Size range (nm)	$\bar{d}$ (nm)
0.05	13.6	0.15	15.7–66.9	31.8(8)
0.10	13.8	0.01	14.8–64.8	30.7(9)
0.15	11.5	0.01	16.1–76.7	32.1(9)
0.20	12.0	0.02	10.7–55.0	29.3(9)

micrographs of the samples alloyed with 5, 10, 15, and 20 at.% of Fe are presented in Figs. 2(a)–2(d). In general, all the samples show similar morphologies. According to the TEM images, ZnO samples were composed of nanoparticles, where each nanoparticle was attached to several other nanoparticles. The TEM observations also showed that ZnO nanoparticles had a spherical shape and were agglomerated to some extent. TEM images were used for the determination of the average size of ZnO nanoparticles. According to the particle size distribution histograms (given in the insets), the particles are homogeneous in size with the dominant particles in the range of about 30 nm (Table I).

D. Magnetic measurements

All measurements of magnetic properties for the investigated samples were made on a commercial SQUID-based magnetometer QD MPMS XL-5. The measurements comprised of temperature dependence of magnetization in both zero field cooled (ZFC) and field cooled (FC) regimes in the wide temperature region of 2–300 K, field dependence of isothermal magnetization at 2 and 300 K as well as AC susceptibility for different field frequencies in the low-temperature region.

Results of ZFC and FC magnetizations vs temperature are shown in Fig. 3. As can be seen, just one sharp maximum at low temperatures of about 10 K exists for each concentration, and no presence of other magnetic phase transitions can be observed.
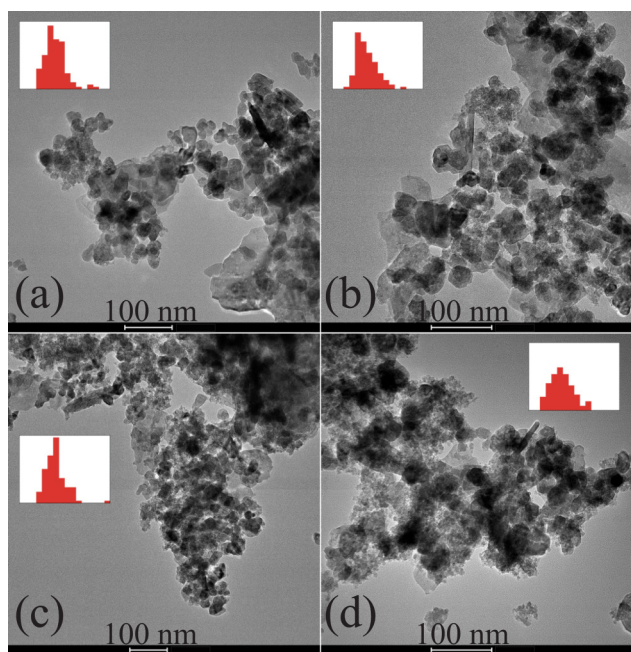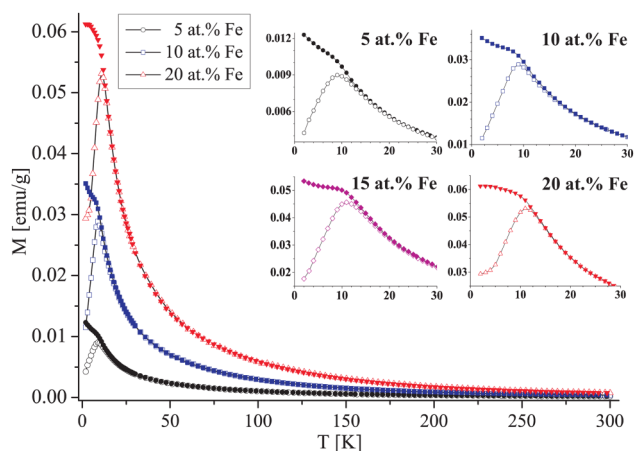

FIG. 3. ZFC (open symbols) and FC (full symbols) magnetization branches recorded in 20 Oe field in 2–300 K temperature range for Fe-alloyed ZnO samples (curve for 15 at.% sample is omitted for clarity). Insets: Low-temperature region with ZFC-FC branches plotted for all the concentrations (lines are just guide for the eye). Shift of the peak position as well as gradual "flattening" of FC branch with increasing Fe ion concentration should be noticed.

Another common property of all the $M(T)$ data is the position of ZFC-FC bifurcation point close to the curve maximum, as well as characteristic λ-shape of the ZFC-FC branches. Such a behavior points to the existence of a low-temperature spin-glass like state in all the samples.[22] Shift of the peak position toward higher temperatures (from 9 K to 11 K for 5 at.% and 20 at.%, respectively) as well as gradual "flattening" of the FC branch is a sign of the magnetic interactions enhancement with the increase of iron concentration.

To verify the presence of a glassy behavior, we conducted both isothermal magnetization vs field measurements below the temperature of the ZFC curve maximum as well as AC susceptibility measurements in the temperature region 5–25 K which encompassed the position of a maximum.

The shapes of the $M(H)$ curves recorded at 2 K depicted in Fig. 4 for samples containing 5 at.% and 20 at.% of iron are similar showing both the presence of hysteresis and absence of saturation at high fields, thus pointing to a glassy nature of magnetic state. Additionally, it should be noted that values of coercivity H_C (denoted in the figure) do not change significantly with the iron concentration x, contrary to magnetization values which scale almost linearly with x. This points to a low distortion of the host wurtzite crystal lattice with increased iron content, thus indicating regular substitution of Zn for Fe. This can also mean that the iron ions are randomly distributed, i.e., no tendency of their agglomeration is observable.

AC susceptibility for both 5 at.% and 20 at.% samples was recorded in zero DC field and 4 Oe AC field amplitude for the field frequencies spanning 1–960 Hz range, in the low-temperature region 5–25 K. Position of the maximum shows frequency dependence and it shifts toward higher temperatures with increased

FIG. 2. TEM micrographs of $Zn_{1-x}Fe_xO$ for x equals (a) 0.05, (b) 0.10, (c) 0.15, and (d) 0.20. The measuring lengths of the micrographs are 100 nm. The insets show the corresponding particle size distribution. The frequency axes (Y) of the distributions have length of 30%, while the particle size axes (X) elongate from 0 to 80 nm.
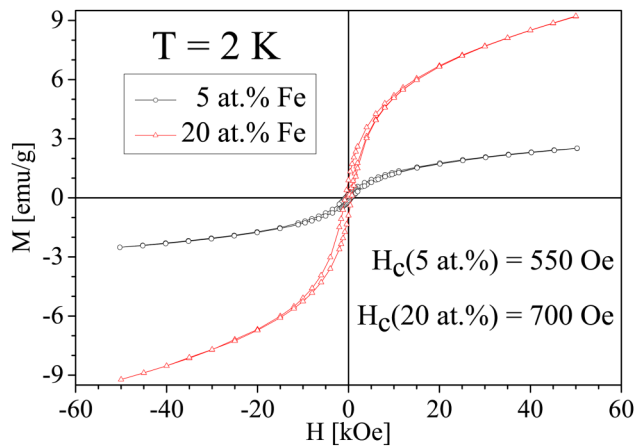
FIG. 4. $M(H)$ curves recorded at $T = 2\,K$ for 5 at.% Fe and 20 at.% Fe samples.
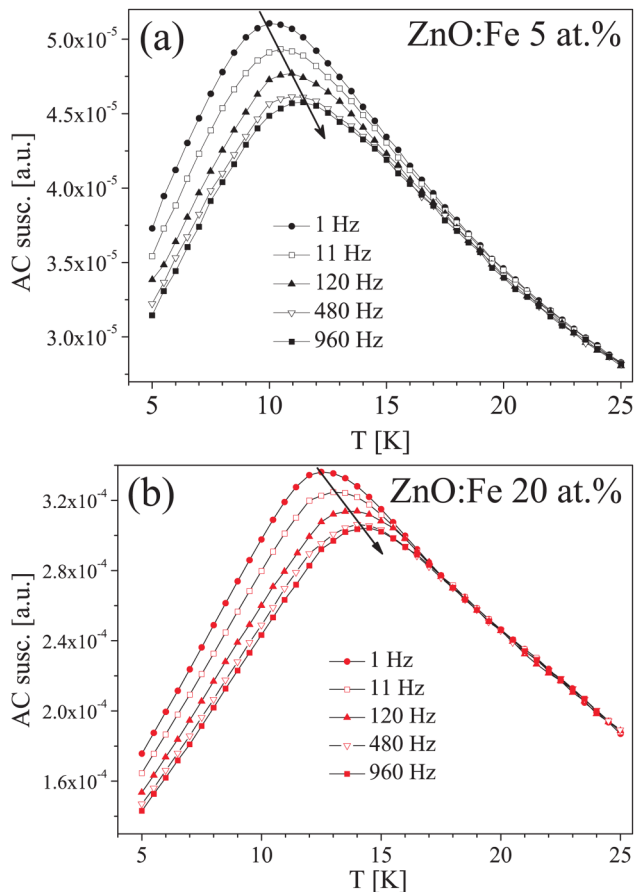

FIG. 5. Low-temperature AC susceptibility of (a) 5 at.%, and (b) 20 at.% Fe containing sample. Arrow shows the direction of the peak shift with increasing frequency.

frequency (Fig. 5). Origin of the shift can be comprehended from the coefficient of the shift $C = \frac{\Delta T}{(T_{av}\Delta \log(f))}$), where ΔT denotes the difference between the peak positions of the highest and lowest frequencies f, while T_{av} is the average value of the peak positions over the applied frequencies.[22]

The so-obtained values $C(5\,\text{at.%}) = 0.046$ and $C(20\,\text{at.%}) = 0.049$ are almost the same, thus pointing to the same origin of magnetic transition point at low temperatures. Both C-values are close to the value of 0.05, which is considered typical of cluster spin-glasses[22] (one should note that for canonical spin-glasses, C is in the range 0.005–0.01, while for interacting superparamagnetic nanoparticles, C is typically in the range 0.01–0.05). Thus, we may conclude that the origin of low temperature magnetic behavior is the formation of the cluster spin-glass state due to the magnetic interaction between iron ions distributed over randomly formed clusters.

To verify the room temperature magnetic behavior we measured $M(H)$ dependences at $T = 300\,K$, and results are shown in Fig. 6. As could be seen from the plotted data, no sign of hysteretic behavior was observed, and for all the samples almost linear M vs H dependence was obtained in the complete field range. This result points to the paramagnetic behavior of the investigated Fe-alloyed ZnO samples at room temperature.

Results of the magnetic measurements show that in all the samples, magnetic properties originate from the atomic (i.e., ionic) magnetism, either in the high temperature region where all the systems are in the paramagnetic state or in the low-temperature region where magnetic interactions between iron ions cause the formation of cluster glass state. The necessary conditions for the latter are: (i) presence of antiferromagnetic (superexchange) interactions among the neighboring iron ions, which may lead to the frustration of the ground state, or (ii) competition between antiferromagnetic and ferromagnetic interactions where the latter may appear due to the F-center exchange mechanism caused by the vacancies/defects in the host lattice.[15,23]
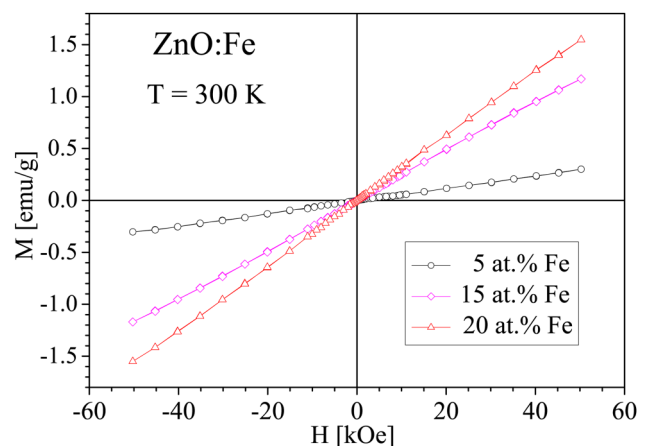

FIG. 6. $M(H)$ data at room temperature for Fe-alloyed ZnO samples (10 at.% sample is omitted for clarity). Lines are just guide for the eye.

E. Measurements of the Mössbauer effect

The measurements of the Mössbauer effect in ZnO nanoparticles were performed in transmission geometry using a $^{57}Co(Rh)$ source at RT. Both software packages, the WinNormos-Site based on the least squares method and the WinNormos-Dist based on the histogram method,[24] were used for the analyses of the measured spectra. During the fitting process, the λ parameter of the maximum entropy method was being varied until the statistical criterion of χ^2 reached the satisfactory value of 1.[25] As the spectrum of the lowest Fe content is characterized with the lowest count rate statistic, we chose $\chi^2 \approx 0.95$. The Wissel spectrometer was calibrated by the spectra of natural iron foil, so the measured isomer shift values are in reference to metallic alpha iron ($\delta = 0$).

The Mössbauer spectra measured at RT for the samples with different nominal concentrations of Fe are presented in Fig. 7. Each of the four spectra consists of paramagnetic doublets. The absence
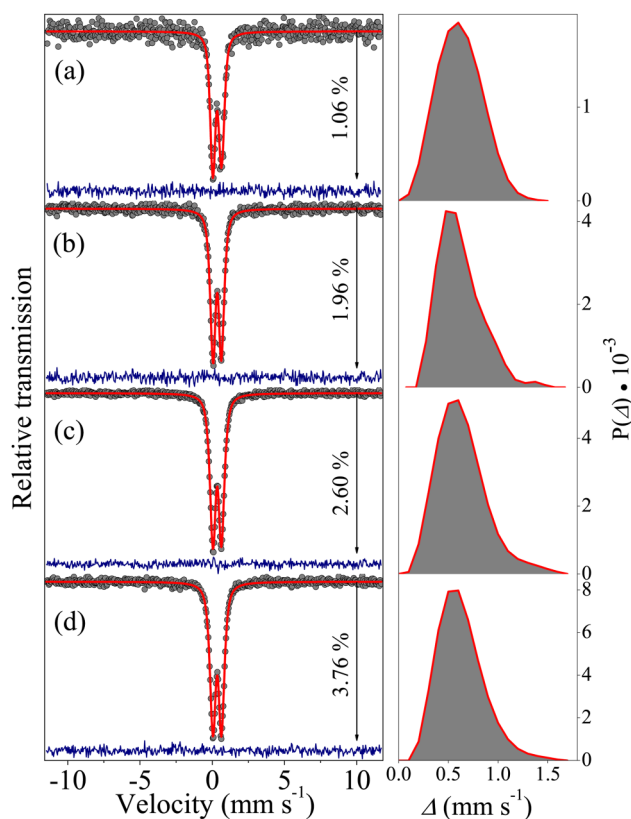

FIG. 7. Mössbauer spectra—on the left side—at $T = 294$ K of the $Zn_{1-x}Fe_xO$ for (a) $x = 0.05$, (b) $x = 0.10$, (c) $x = 0.15$, and (d) $x = 0.20$. The experimental data are presented by solid gray circles and the fit is given by the solid red line. Vertical arrow denotes the relative position of the lowermost peak with respect to the basal line (Relative transmission). The difference (Th − Exp) is shown below the main spectrum. The |Th − Exp| is less than (a) 0.115%, (b) 0.094%, (c) 0.105%, and (d) 0.174%. The corresponding distributions of the quadrupole splittings are presented on the right side.

of any sextet rules out the existence of iron oxides as well as metallic iron structures in the samples.[26] Beltrán et al.[13] and Limaye et al.[15] suggested that increasing of Fe concentration leads to an antiferromagnetic superexchange coupling between the neighboring Fe spins, which is the dominant interaction at low-temperature confirmed by our magnetic measurements. On the other side, ferromagnetic phenomenon may have origin in an exchange interaction via trapped electron in hole.[27] Such local arrays would produce the Zeeman effect at the Fe nuclei and as stated above, this was not observed in our samples. The mean lifetime (140 ns) of the excited ^{57}Fe-Mössbauer state is too long for observing a magnetic hyperfine interaction in these $3d$-doped systems with the present impurity concentrations. An extremely diluted regime of the Fe ions in ZnO is characterized by spin-lattice relaxation with a long relaxation time. As the concentration of $3d$-spins increases, the strong spin-spin relaxation becomes predominant, so the spin-spin relaxation rate increases.[28] The magnetic measurements show that all the samples at RT are in the paramagnetic state, so the probes detect fast paramagnetic relaxations ($>10^{12}$ Hz).[29]

In order to explain the measured spectra, it is necessary to review possible crystal structure sites, which could be occupied by the Fe ions. It has been determined that the Fe ions in Fe-alloyed ZnO usually replace Zn^{2+} at the tetrahedral site with the $3m$ point group symmetry (ditrigonal-pyramidal). The earlier measured values of isomer shift (δ) and quadrupole splitting (Δ) indicate that the Fe ions are in the 3+ valence state with spin $S = 5/2$.[11,13,15,19] A neutralization of the charge imbalance due to the charge mismatch of the substituent and the host cations occurs by creation of the cationic vacancies V_{Zn}.[11,14] It is worth mentioning that the main contribution to the values of hyperfine parameters comes from the first coordination sphere (ICS), while a strong influence of the second CS (IICS) is only represented by modifying ICS electron density. ICS of a Zn ion consists of four oxygen ions making ZnO_4 tetrahedron. Three Zn–O bonds are the same making a base of the tetrahedron, whereas the fourth oxygen at the apical position is bounded at a somewhat different distance. The next nearest neighbors are 12 Zn ions distributed into two Zn-subshells around the central Zn ion. Two subshell distances from the central Zn ion differ for approximately 1.2%. Three basal oxygen ions are bonded with one zinc ion from the I subshell and two zinc ions from the II subshell, whereas the apical anion binds three cations from the I Zn-subshell. Replacing the Zn ion by the Fe ion leads to a local symmetry breaking. This is reflected in the change of the Fe–O bond lengths and the distances between the central Fe cation and Zn cations from the IICS. Works of Rita et al.[30] and Pereira et al.[31] point out that the mean squared displacement of the substituted iron from the ideal lattice site position is at least 0.06–0.09 nm. The displacement value depends on the design and temperature treatment of samples. Such an environment provides an electric quadrupole interaction between electric field gradient (EFG) and the electric quadrupole moment of the nucleus (Q). This interaction can be described by the principle component of the diagonalized EFG tensor V_{zz}, and the asymmetry parameter $\eta = \left| (V_{yy} - V_{xx})/V_{zz} \right|$. One of the ways for measuring this interaction is Mössbauer effect spectroscopy, which is an investigation tool that can clearly give either a valence state of the Fe ions or their coordination numbers. The resulted shape of the Mössbauer

TABLE II. The fitted Mössbauer hyperfine parameters of $Zn_{1-x}Fe_xO$ at 294 K using the WinNormos-Dist option: x—nominal amount of Fe; CR (relative transmission)—count rate expressed in the unit of σ; Δ—statistical average quadrupole splitting value; SD—standard deviation; Skew—skew of distribution; Kurtosis—kurtosis of distribution; UT—unimodal tendency; $\bar{\delta}$—statistical average isomer shift value. The fitting errors are presented in parentheses.

x	CR[a] (σ)[b]	$\bar{\Delta}$ (mm s^{-1})	SD (mm s^{-1})	Skew	Kurtosis	UT	$\bar{\delta}$ (mm s^{-1})
0.05	23.0	0.616	0.225	0.248	−0.265	0.674	0.345(13)
0.10	48.4	0.619	0.219	0.837	0.752	1.051	0.345(5)
0.15	81.1	0.633	0.252	0.810	0.914	1.258	0.343(3)
0.20	63.7	0.628	0.233	0.770	0.832	1.239	0.343(5)

[a]Expressed in signal to noise ratio.
[b]The standard deviation of background.

spectrum is named doublet. The symmetry of the Fe probe site (Fe_{Zn}) additionally breaks when a vacancy V_{Zn} takes place in the IICS. There are several positions where V_{Zn} can appear—one might expect the joint effect on the doublet through its wider line and higher Δ uncertainty. Vacancies from the IICS deteriorate the Fe tetrahedron regularity making it tilted. This is reflected in the higher values of V_{zz} and η giving higher Δ values. A large number of the nonequivalent Fe sites may occur when a possibility of the random spreading V_O over the lattice is added. Hence, we selected a distribution of quadrupole splittings as a fitting model of our spectra. The results are shown in Table II.

The right side of Fig. 7 shows the obtained distribution functions. All the distributions contain a prominent maximum accompanied by a right tail. A deviation from the standard (Gaussian) distribution is expressed by higher moments of the distribution function.[25] Coefficient of skewness (skew) is the third centered moment, where the positive value expresses the longer right tail than the left one (vice versa for the negative skew). Kurtosis is the fourth centered moment. The positive kurtosis means that there is a heavy-tailed distribution, flatter than the standard distribution. The case of kurtosis < 0 specifies a light-tailed distribution with the more pointed peak with respect to the standard distribution.[25] All the obtained skews are positive indicating that the distributions cover the doublets with the greater Δ values (Table II). The negative kurtosis and the small skew for $x = 0.05$ points out that the Mössbauer responses come mainly from Fe_{Zn} followed by one V_{Zn} in the IICS. Going from the $x = 0.05$ to 0.15, the kurtosis, the unimodal tendency, and the statistical average Δ ($\bar{\Delta}$) increase, letting us know that the doublets, which originate in both the Fe_{Zn} with more than one V_{Zn} (or at least one V_{Zn} coupled with another Fe_{Zn}) in the IICS and the Fe_{Zn} accompanied by V_O in the ICS, take place in the distribution with greater weights. Also, the increase of $\bar{\Delta}$ could be related to the r^{-3} dependence of V_{zz} due to the decrease of the lattice parameters with the increase of the amount of Fe.[13] The shape of the particle size distribution of the 10 at.% Fe-alloyed ZnO depicted in Fig. 2(b) indicates that the larger particles prevail over the smaller ones. This could be related to the smallest value of the standard deviation of the quadrupole distribution for 10 at.% Fe (Table II), and vice versa in the case of 15 at.% Fe.

In the case of $x = 0.20$, one could expect the further increase in values of both the hyperfine parameter and the coefficients of the distribution because more Fe ions produce more vacancies. In order to explain the unexpected results, first, it is worth noting that the chemical kinetics of the Fe–Zn–O system favors the formation of the more stable $ZnFe_2O_4$ compound instead of any of the iron oxides as spurious phases.[32] This phase is generally formed either at greater iron concentration or with increasing processing temperature and duration.[31] The Mössbauer response from the Fe^{3+} at the octahedral sites in a normal spinel $ZnFe_2O_4$ nanopowder (the δ in the range of 0.34–0.36 mm s^{-1} at RT; the Δ values of 0.39–0.60 mm s^{-1}) could overlap the response from Fe^{3+}_{Zn} in the investigated Fe-ZnO phase.[13,32,33] Hence, this minute contribution of the unwanted impurity phase has a minor contribution to the left side of the distribution. This consideration leads us to confirm the claim of Mandal *et al.*[34] that the solubility limit of Fe in ZnO at RT is nearly 20%. Besides, Beltrán *et al.*[13] found that most of the V_{Zn} are located in the particle shell, indicating that the average particle size decreases. Therefore, the surface area increases with increasing Fe content. This might favor fewer numbers of multiple V_{Zn} environments at bigger Fe concentrations (according to the skew, it already happens at $x \geq 0.15$ in our case).

As all the histogram doublet isomer shifts belong to the range of 0.321–0.379 mm s^{-1} [the largest relative uncertainty of statistical average δ ($\bar{\delta}$) is less than 3.8%], we find that the observed values for δ are somewhat higher than usual for the 4-fold coordinated Fe^{3+}. The larger δ is caused by the lower s-electron charge density at the ^{57}Fe nucleus. Indirect contribution occurs by changing the shielding effect on s-electron through the decrease of the $3d$-electron density caused by the $3d$–$2p$ hybridization. Direct contribution is due to diminishing the $4s$-electron density as consequence of the $4sp$–$2p$ hybridization.[14]

III. FIRST-PRINCIPLES CALCULATIONS

A. Calculation procedure

All calculations were performed using the (linearized) augmented plane waves + local orbitals [(L)APW + lo] method based on DFT, as implemented in WIEN2k code.[35] In this method, the unit cell is divided into nonoverlapping muffin-tin spheres around atoms, in which the wave functions are expanded in spherical harmonics and an interstitial region where they are expanded in plane waves. The muffin-tin radii for Zn and Fe were 1.7 a.u. and for O atom 1.6 a.u. In our spin polarized calculations, the cut-off parameter $RMTk_{max}$ for limiting the number of plane waves, where RMT

is the smallest of all the muffin-tin spheres and k_{max} is the largest reciprocal lattice vector used in the plane wave expansion, was chosen to be 8. The charge density was Fourier expanded up to $G_{max} = 16$. The core-valence state separation was settled at -7 Ry. The core states were treated fully relativistically, while the valence states were treated within the scalar relativistic approximation.

We first optimized volume, c/a ratio, and internal structural parameters of ZnO with PBE-GGA[36] exchange-correlation potential and then constructed a $2 \times 2 \times 2$ supercell (32 atoms) from periodically repeating unit cells. After that, one Zn atom was replaced by Fe to simulate Fe cation substituted ZnO, which corresponded to $Zn_{0.9375}Fe_{0.0625}O$. To model the V_O and the V_{Zn}, one nearest neighbor oxygen and one next nearest neighbor zinc atom around Fe were removed, respectively. The V_O was created along the z-axis with respect to the Fe atom, because it was shown earlier that this is the configuration with the lowest formation energy.[37] The supercells used in our study are shown in Fig. 8.[38] The Brillouin zone (BZ) integration was achieved via a tetrahedron method,[39] using 24 k points in the irreducible wedge of the Brillouin zone. In all our calculations, the charge convergence criterion was employed, demanding the charge difference between the iterations to be smaller than 10^{-5} electrons. The calculated isomer shift (δ_c) was evaluated from the self-consistent electron density using the procedure described in Ref. 40. The EFG tensor was obtained from the calculated self-consistent charge density by solving the Poisson's equation directly.[41,42] The largest component of the EFG tensor was then designated as V_{zz} and the asymmetry parameter η was calculated as $\eta = \left|\left(V_{yy} - V_{xx}\right)/V_{zz}\right|$. In order to estimate the values of calculated quadrupole splitting (Δ_c), the energy difference between the ^{57}Fe ($|I = 3/2\rangle$) sublevels is used,[43]

$$\Delta_c = \frac{1}{2} eQ V_{zz} \sqrt{1 + \frac{\eta^2}{3}}. \qquad (1)$$

We utilize the ^{57}Fe nuclear electric quadrupole moment value of $Q = 0.16$ b.[44] In ^{57}Fe-Mössbauer spectroscopy, $1\,mm\,s^{-1}$ is $48.075\,neV$.[43] The Fermi contact term, which gives dominant contribution to the hyperfine magnetic field (B_{hf}), was determined from the spin density at the nucleus in the scalar-relativistic
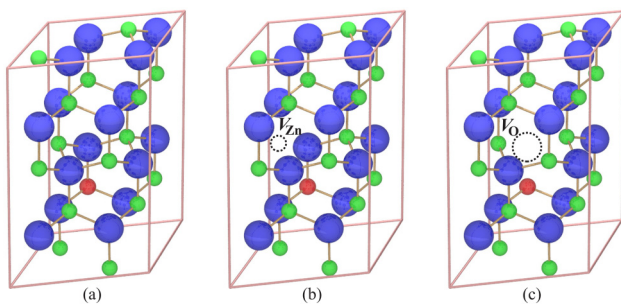

FIG. 8. Models of cells used for the calculations. Zinc (oxygen) ions are depicted by green (blue) balls while iron probe is shown by red ball. Vacancies are depicted by dash circles.

approximation.[45,46] Apart from the neutral, the charged supercells were also considered, as it was demonstrated earlier[47] that the charge state of impurity must be taken into account when calculating EFGs of metal impurities in oxide semiconductors.

B. Calculation results

In the pure wurtzite ZnO, the first coordination shell around each Zn atom consists of three O atoms at the distance 1.998 Å and one O atom at 2.016 Å, while the second coordination sphere contains six Zn atoms at the distance 3.249 Å and another six Zn atoms at the distance of 3.289 Å. After substituting one Zn atom in the cell with Fe, a shortening of interatomic distances in both the first and the second coordination shell is observed (Table III). Upon including the native point defects V_{Zn} and V_O, the shortening becomes even more pronounced.

The calculated V_{zz}, η, as well as B_{hf}, in Fe cation substituted ZnO, with and without point defects, are shown in Table IV. For comparison with the measured data from Mössbauer spectroscopy, the values of Δ_c estimated according to Eq. (1) are also shown in Table IV. For the sake of clarity, it is worth keeping in mind that the measured isomer shift consists of two terms, $\delta = \delta_{CS} + \delta_{SOD}$. The first is a chemical shift, whereas the second has the opposite sign and originates in the second order Doppler shift.

IV. DISCUSSION

As the iron concentration in our calculated system was $x = 0.0625$, we compared our calculated values with the measured ones for the smallest Fe concentration. The $\bar{\Delta}$ value of $0.616\,mm\,s^{-1}$ (Table II) well agrees with our calculated values for the Δ_c at both the basal and the apical Fe position with V_{Zn} in the IICS environment (C5 and C6 from Table IV). Here, we must take into consideration a V_{zz} trend to decrease with an increase of T. While δ_c of $0.41\,mm\,s^{-1}$ for the apical Fe cation substituted ZnO with V_{Zn}^0 (C6) excellently corresponds to $\bar{\delta}$, there is discrepancy in the case of the basal Fe cation substituted ZnO with V_{Zn}^0 (C5). Calculated total energy favors the basal case (C5) with respect to the apical one (C6) by 0.0156 eV/atom. Hence, we could not exclude that the Mössbauer responses come from both sites recorded at RT with very similar values of Δ. The value of $0.06\,mm\,s^{-1}$ (it is less at RT) is not common for the δ of the ^{57}Fe where the coordination number is four, so we declare that δ_c is underestimated. The V_O^{2+} in the ICS (C4) causes the Δ_c of

TABLE III. The interatomic distances in Fe cation substituted ZnO (Fe-ZnO) for different investigated systems.

System	d_{Zn-O} (Å)	d_{Zn-Zn} (Å)
Pure ZnO	1.998	3.249
Fe-ZnO neutral	1.986	3.209
Fe-ZnO with V_O^0	1.992	3.018
Fe-ZnO with V_O^{2+}	1.912	2.885
Fe-ZnO with V_{Zn}^0	1.932	3.166
Fe-ZnO with V_{Zn}^{2-}	1.906	3.155

TABLE IV. The hyperfine interactions parameters in Fe cation substituted ZnO (Fe-ZnO) for different investigated systems: δ_c—calculated isomer shift; V_{zz}—principle component of the diagonalized EFG tensor; η—asymmetry parameter; Δ_c—calculated quadrupole splitting; B_{hf}—hyperfine magnetic field; μ_{Fe}—magnetic moment per iron atom.

System	δ_c (mm s^{-1})	$V_{zz} \times 10^{-21}$ (V m^{-2})	η	Δ_c (mm s^{-1})	B_{hf} (T)	μ_{Fe} (μ_B)
Basal Fe-ZnO neutral—C1	0.68	−8.6	0.293	−1.451	−27.4	3.48
Apical Fe-ZnO neutral—C2	0.69	9.9	0.010	1.647	−27.5	3.47
Fe-ZnO with V_O^0—C3	0.77	12.2	0.276	2.056	−22.2	3.23
Fe-ZnO with V_O^{2+}—C4	0.38	7.8	0.002	1.298	−29.2	3.35
Basal Fe-ZnO with V_{Zn}^0—C5	0.06	4.5	0.456	0.774	−21.7	2.96
Apical Fe–ZnO with V_{Zn}^0—C6	0.41	−5.0	0.305	−0.845	−28.0	3.62
Fe-ZnO with V_{Zn}^{2-}—C7	0.62	−6.5	0.422	−1.113	−26.1	3.39

≈ 1.3 mm s^{-1} at the ^{57}Fe nuclei as it is observed in the distribution tails—see Fig. 7. The corresponding δ_c of 0.38 mm s^{-1} is smaller than the value in the case of the apical Fe$_{Zn}$ with V_{Zn}^0 (C6). The very slight decline of $\bar{\delta}$ (values overlapping in their uncertainty ranges, Table II) might be connected with a somewhat greater presence of these defects for larger x.

According to our calculations, there are several candidates (C1, C2, C3, and C7) that could account for contribution with larger Δ. Among the main ones are the defect-free charge neutral configurations where the Zn ion is replaced by the Fe ion either at the basal (C1) or at the apical (C2) site. The Δ_c value of 1.451 mm s^{-1} for the C1-configuration agrees very well with the component observed in many earlier Mössbauer measurements of Fe-doped ZnO. For instance, it was observed in Ref. 8 and it was correctly ascribed to the case when a Fe atom replaces a Zn in the defect-free ZnO. Even the Fe charge state confirms this as the measured component that corresponds to the Fe^{2+} state, which is exactly the case when a Fe atom replaces a Zn in the defect-free Zn^{2+}O^{2-} in the neutral cell (C1 and C2). In the case of the Fe alloying in the presence of V_O in ZnO (C3), our Δ_c value at Fe position of 2.056 mm s^{-1} corresponds to the component of the Mössbauer spectrum with Fe^{3+} state observed in Ref. 12. As the observed Fe valences in our experiments are 3+, this condition disqualifies all the other calculated configurations (C1, C2, C3, and C7). According to our experimental experience, the values of δ_c are underestimated for the 4-fold coordinated Fe^{2+} ions.

In order to parse the distributions into Lorentz line doublets, we used two doublet fitting model. The results are shown in Table V. Similar results were published earlier for sample prepared by the same method.[15] Also, a similar larger Δ component was observed in a number of earlier reported Mössbauer spectra[8,9,12,17] in the samples obtained by chemical, self-combustion, microwave-assisted, and solid-state reaction methods, with up to 5% of Fe and it was tentatively ascribed to Fe atoms in the vicinity of V_{Zn}.[8] As we stated above, this component can be confirmed by our calculations. Small differences for the Δ_c values of this component in different samples can partly be explained by the differently calculated quadrupole splitting values when the Fe atom replaces in-plane and apical Zn atoms and also by the different c/a ratio for the samples obtained using different methods. On the other side, the second Mössbauer component of the smaller Δ does not match any of the

investigated cases (Fe cation substituted in defect-free ZnO, with one nearest neighbor oxygen and one next nearest neighbor zinc ZnO). To test the obvious possibility that the charge state of the impurity-host system was responsible for this discrepancy, we also performed calculations for the charged supercells (C7), taking into account the well-known charge states of particular defects in ZnO (2+ or neutral for V_O and 2− for V_{Zn}) from the literature.[48] From Table IV, we can see that the calculated V_{zz} at Fe in the double charged cell with V_O is smaller than in the neutral case. The corresponding Δ_c value can be compared with the measured RT value of 1.28 mm s^{-1} (sign undetermined) from Ref. 17, in which Zn$_{0.95}$Fe$_{0.05}$O sample was made by the hydrothermal method. However, the component with smaller Δ cannot be accounted for based on the investigated cases. It is highly unlikely that the local symmetry of probe may improve following the increased number of defects in its environment. Allowing that every Fe site has the same recoil-less factor, there could be expected constant decline (decrease) of the relative doublet area depending on the x. Such a trend is not evident from Table V. Considering these facts we conclude that the narrow doublet is fake (ghost doublet). Hence, we recommend that two doublet fitting model has to be rejected. There is only one main doublet accompanied by contributions

TABLE V. The fitted Mössbauer hyperfine parameters of Zn$_{1−x}$Fe$_x$O at 294 K using the WinNormos-Site in the thin absorber approximation mode: x—nominal amount of Fe; χ^2—goodness of fit; A—relative area of subspectrum; Γ—line width; δ—measured isomer shift; Δ—quadrupole splitting. The fitting errors are presented in parentheses.

x	χ^2	A (%)	Γ (mm s^{-1})	δ (mm s^{-1})	Δ (mm s^{-1})
0.05	0.940	40(10)	0.28(4)	0.331(7)	0.42(3)
		60(10)	0.35(3)	0.352(5)	0.75(4)
0.10	1.015	64(9)	0.33(2)	0.344(2)	0.49(2)
		36(10)	0.35(3)	0.348(3)	0.82(4)
0.15	0.972	59(6)	0.34(1)	0.342(1)	0.49(1)
		41(6)	0.39(1)	0.345(2)	0.83(3)
0.20	0.994	70(7)	0.36(1)	0.344(1)	0.51(2)
		30(7)	0.36(3)	0.343(3)	0.87(3)

from the right side of the energy axis. So, the histogram fitting model is a suitable tool for our recorded spectra.

The calculated B_{hf} at the Fe nucleus are also shown in Table IV. They reflect the s-electrons polarization and consist of a valence and a core contribution. In all the investigated systems, the core contribution is larger and of opposite sign with respect to the valence contribution. The fact that Mössbauer spectroscopy shows no detectable B_{hf}, while the calculations predict sizeable B_{hf}, can be explained by the strong spin fluctuations in this system characterized by a time τ_R much shorter than ^{57}Fe-Mössbauer measurement time of $\sim 10^{-7}$ s. Additionally, there is the fact that the Mössbauer spectra were measured at RT, whereas the calculations reflect the situation at 0 K. However, in some of the earlier reported Mössbauer measurements[49] on the samples obtained by ion implantation, where the hyperfine parameters were measured at the ^{57}Fe probe site produced by the β decay of ^{57}Mn, components of the Mössbauer spectrum with nonzero B_{hf} were detected. One of those components, corresponding to a high-spin Fe^{3+} state, with the Δ_c value of -0.845 mm s^{-1}, exactly matches our calculated Δ_c for the apically Fe cation substituted ZnO with V_{Zn} in the IICS environment (C6), but the corresponding B_{hf} differ for about 25%. Actually, a sextet could be recorded only for a very low concentration of the iron dopant.[28,29,50–53] All the sextets obtained by emission Mössbauer spectroscopy (eMS) suffer from a line-broadening due to relaxation effects. Their origin is in $Fe^{3+}_{Zn}-V_{Zn}$ defect complexes. In this complex, there is a weak spin-lattice interaction between the lattice and the ^{6}S ground state of Fe^{3+} with an exceptionally long relaxation time of up to 10^{-5} s at RT.[28,50,52,53] This complex ($Fe^{3+}_{Zn}-V_{Zn}$ pair) might be the reason for the 3+ valence of the Fe ions instead of the formation of the deep charge compensating defects.[49,52] Mantovan et al.[28] proposed the limit of 0.22 at.% of iron in ZnO as a threshold when the strong spin-spin relaxation between $Fe^{3+}-Fe^{3+}$ ions emerges. Even if the spin-spin interaction time is long enough, the appearance of the sextets in our spectra would be questionable due to the size of the crystallites (Table I). A very high spin-spin relaxation rate is the reason why the observed Fe^{3+} doublet by Ahn et al. at 13 K[17] and by Mishra and Das at 20 K[11] did not transform into a sextet.

A lot of research was conducted at the ISOLDE facility at CERN by eMS on the Fe ions implanted into ZnO monocrystal. Gunnlaugsson et al.[29] measured Fe^{3+}-paramagnetic doublet of $\delta = 0.41$ mm s^{-1} and $\Delta = -0.652$ mm s^{-1}, which is almost the same as our result. The central part of the eMS spectra is dominated by the presence of the Fe^{2+}_{Zn}-paramagnetic doublet.[28,29,50–53] The tetrahedral position of the Fe^{2+} is characterized by δ of $0.85-0.91$ mm s^{-1} and unexpectedly very small values for Δ less than 0.4 mm s^{-1}.[51,52] It is to be expected that Fe^{2+} at the ditrigonal-pyramidal site should have as large quadrupole splitting as our calculations yield, the values of C1 and C2 in Table IV. All this brings us to the conclusion that a displacement of the Fe ion from the regular Zn site[30,31] leads to the more spherical distribution of electron density of the Fe^{2+}. There is an empty octahedral interstitial site in the ZnO with the wurtzite structure which can be populated by either substituting zinc atom of the 2+ valence or iron atom of the 3+ valence.[54,55] The measured doublets in eMS experiments have the values of δ of $0.50-0.56$ mm s^{-1} and Δ of $0.85-0.90$ mm s^{-1}.[51,52] Using the Lorentz-doublet fitting model,

first we put the starting fitting parameters of Fe^{2+}-doublet similar to the parameters quoted in Refs. 51 and 52. This kind of fitting procedure failed for all our four spectra. So, we can conclude that there is no evidence of the Fe^{2+} ions in the investigated Mössbauer spectra. Otherwise, we cannot exclude that the quadrupole distributions cover a small amount of the interstitial Fe^{3+} ions.

If we compare our calculated results with the calculations reported earlier,[56] we observe excellent agreement with the calculated B_{hf} at Fe atom in the Fe cation substituted ZnO, but a large difference in the calculated Δ_c values. This is probably not surprising given that the Δ_c values are more susceptible to changes in the lattice structure and the c/a ratio than the B_{hf}. Also, we computed the quadrupole frequency (ν_Q) at ^{67}Zn and compared it with the results of the measurements of ZnO single crystal at 4.2 K obtained by the ^{67}Zn-Mössbauer spectroscopy.[57] To calculate V_{zz} ($h\nu_Q = eQV_{zz}$) from the measured result of 2.401 MHz, we used the value of $Q(|I = 5/2^-\rangle)$ of 0.15 b.[58] The very stable low-temperature V_{zz} of 6.62×10^{20} V m^{-2}[57] is in very good agreement with our calculated one of 8×10^{20} V m^{-2} for the vacancy free ZnO.

V. CONCLUSION

In summary, we used Mössbauer spectroscopy and the first-principles calculations of hyperfine interaction parameters to study the local structure and defects formation in Fe-alloyed ZnO obtained by microwave processing. We found paramagnetic doublets, with no trace of a sextet. The distribution of quadrupole splittings as a fitting model is required for the analysis of the Mössbauer spectrum instead of the two Lorentz-doublet fitting model. The ab initio calculations confirmed that the main contributing component of the Mössbauer spectra corresponds to the Fe cation substituted ZnO with Zn vacancy in the next nearest neighbor environment and helped identify some of the components from the earlier reported Mössbauer measurements in the samples obtained by different methods.

The microwave method introduces a lot of vacancies during the synthesis, which facilitates the creation of $Fe^{3+}_{Zn}-V_{Zn}$ pairs. Mössbauer spectroscopy reveals that the majority of the iron ions in ZnO synthesized by the microwave method is the Fe^{3+} ions. Actually, our Mössbauer spectra do not give an evidence of the existing high-spin Fe^{2+} ions in the samples. The magnetic measurements indicate that the microwave method provides random distribution of iron atoms over the lattice without their agglomeration except for the sample with 20 at.% Fe where they segregate into the impurity phase.

REFERENCES

[1] A. Kołodziejczak-Radzimska and T. Jesionowski, Materials 7, 2833 (2014).
[2] A. Djurišić, A. Ng, and X. Chen, Prog. Quant. Electron. 34, 191 (2010).
[3] S. García-Rodríguez, "Alternative metal oxide photocatalysts," in Design of Advanced Photocatalytic Materials for Energy and Environmental Applications,

Green Energy and Technology, edited by J. Coronado, F. Fresno, M. Hernández-Alonso, and R. Portela (Springer, London, 2013), Vol. 71, Chap. 6, pp. 103–108.

[4]L. Xu and X. Li, J. Cryst. Growth **312**, 851 (2010).

[5]M. Venkatesan, C. B. Fitzgerald, J. G. Lunney, and J. M. D. Coey, Phys. Rev. Lett. **93**, 177206 (2004).

[6]A. K. Yadav, S. M. Haque, S. Tripathi, D. Shukla, M. A. Ahmed, D. M. Phase, S. Bandyopadhyay, S. N. Jha, and D. Bhattacharyya, RSC Adv. **6**, 74982 (2016).

[7]S. Katba, S. Jethva, M. Udeshi, P. Trivedi, M. Vagadia, D. Shukla, R. Choudhary, D. Phase, and D. Kuberkar, Appl. Surf. Sci. **423**, 100 (2017).

[8]D. Karmakar, S. K. Mandal, R. M. Kadam, P. L. Paulose, A. K. Rajarajan, T. K. Nath, A. K. Das, I. Dasgupta, and G. P. Das, Phys. Rev. B **75**, 144404 (2007).

[9]H. Liu, J. Yang, Y. Zhang, Y. Wang, and M. Wei, Mater. Chem. Phys. **112**, 1021 (2008).

[10]H. Liu, J. Yang, Y. Zhang, L. Yang, M. Wei, and X. Ding, J. Phys. Condens. Matter **21**, 145803 (2009).

[11]A. Mishra and D. Das, Mater. Sci. Eng. B **171**, 5 (2010).

[12]R. Saleh, S. P. Prakoso, and A. Fishli, J. Magn. Magn. Mater. **324**, 665 (2012).

[13]J. J. Beltrán, C. A. Barrero, and A. Punnoose, Phys. Chem. Chem. Phys. **17**, 15284 (2015).

[14]S. Kumar, Y. J. Kim, B. H. Koo, S. K. Sharma, J. M. Vargas, M. Knobel, S. Gautam, K. H. Chae, D. K. Kim, Y. K. Kim, and C. G. Lee, J. Appl. Phys. **105**, 07C520 (2009).

[15]M. V. Limaye, S. B. Singh, R. Das, P. Poddar, and S. K. Kulkarni, J. Solid State Chem. **184**, 391 (2011).

[16]I. Lorite, Y. Kumar, P. Esquinazi, S. Friedländer, A. Pöppl, T. Michalsky, J. Meijer, M. Grundmann, T. Meyer, and I. Estrela-Lopis, Appl. Phys. Lett. **109**, 012401 (2016).

[17]G. Y. Ahn, S.-I. Park, I.-B. Shim, and C. S. Kim, J. Magn. Magn. Mater. **282**, 166 (2004), International Symposium on Advanced Magnetic Technologies.

[18]A. Samariya, R. Singhal, S. Kumar, Y. Xing, M. Alzamora, S. Dolia, U. Deshpande, T. Shripathi, and E. B. Saitovitch, Mater. Chem. Phys. **123**, 678 (2010).

[19]M. Carvalho, L. Ferreira, R. Borges, and M. Godinho, J. Solid State Chem. **185**, 160 (2012).

[20]R. W. Cheary and A. Coelho, J. Appl. Crystallogr. **25**, 109 (1992).

[21]W. Rasband, "ImageJ," U.S. National Institutes of Health, Bethesda, Maryland, USA (1997–2012).

[22]J. A. Mydosh, Spin Glasses: An Experimental Introduction (Taylor & Francis, London, 1993).

[23]J. M. D. Coey, A. P. Douvalis, C. B. Fitzgerald, and M. Venkatesan, Appl. Phys. Lett. **84**, 1332 (2004).

[24]R. Brand, WinNormos Mössbauer Fitting Program (Universität Duisburg, Duisburg, 2008).

[25]R. Brand and G. L. Caër, Nucl. Instrum. Methods B **34**, 272 (1988).

[26]E. Murad and J. Cashion, Mössbauer Spectroscopy of Environmental Materials and Their Industrial Utilization (Springer, New York, 2004).

[27]K. Sato and H. Katayama-Yoshida, Jpn. J. Appl. Phys. **40**, L334 (2001).

[28]R. Mantovan, H. P. Gunnlaugsson, K. Johnston, H. Masenda, T. E. Mølholt, D. Naidoo, M. Ncube, S. Shayestehaminzadeh, K. Bharuth-Ram, M. Fanciulli, H. P. Gislason, G. Langouche, S. Ólafsson, L. M. C. Pereira, U. Wahl, P. Torelli, and G. Weyer, Adv. Electron. Mater. **1**, 1400039 (2015).

[29]H. P. Gunnlaugsson, K. Johnston, T. E. Mølholt, G. Weyer, R. Mantovan, H. Masenda, D. Naidoo, S. Ölafsson, K. Bharuth-Ram, H. P. Gíslason, G. Langouche, M. B. Madsen, and the ISOLDE Collaboration, Appl. Phys. Lett. **100**, 042109 (2012).

[30]E. Rita, U. Wahl, J. G. Correia, E. Alves, and J. C. Soares, Appl. Phys. Lett. **85**, 4899 (2004).

[31]L. M. C. Pereira, U. Wahl, J. G. Correia, M. J. V. Bael, K. Temst, A. Vantomme, and J. P. Araújo, J. Phys. Condens. Matter **25**, 416001 (2013).

[32]G. F. Goya and E. R. Leite, J. Phys. Condens. Matter **15**, 641 (2003).

[33]Z. Ž. Lazarević, Č. Jovalekić, V. N. Ivanovski, A. Rečnik, A. Milutinović, B. Cekić, and N. Ž. Romčević, J. Phys. Chem. Solids **75**, 869 (2014).

[34]S. K. Mandal, A. K. Das, T. K. Nath, and D. Karmakar, Appl. Phys. Lett. **89**, 144105 (2006).

[35]P. Blaha, K. Schwarz, G. Madsen, D. Kvasnicka, and J. Luitz, "Wien2k, an augmented plane wave + local orbitals program for calculating crystal properties," Karlheinz Schwarz, Techn. Universität Wien, Austria, 2001. ISBN 3-9501031-1-2.

[36]J. P. Perdew, K. Burke, and M. Ernzerhof, Phys. Rev. Lett. **77**, 3865 (1996).

[37]A. Debernardi and M. Fanciulli, Physica B **401**, 451 (2007).

[38]V. Luaña, "Tessel version 2.1," Quantum Chemistry Group, Departamento de Química Física y Analítica, Universidad de Oviedo, Oviedo, Spain, 1996–2003.

[39]P. E. Blöchl, O. Jepsen, and O. K. Andersen, Phys. Rev. B **49**, 16223 (1994).

[40]P. Blaha, J. Phys. Conf. Ser. **217**, 012009 (2010).

[41]P. Blaha, K. Schwarz, and P. Herzig, Phys. Rev. Lett. **54**, 1192 (1985).

[42]K. Schwarz, C. Ambrosch-Draxl, and P. Blaha, Phys. Rev. B **42**, 2051 (1990).

[43]Yi.-L. Chen and D.-P. Yang, Mössbauer Effect in Lattice Dynamics: Experimental Techniques and Applications (Wiley, Weinheim, 2007), pp. 9–41.

[44]P. Dufek, P. Blaha, and K. Schwarz, Phys. Rev. Lett. **75**, 3545 (1995).

[45]T. Korhonen, A. Settels, N. Papanikolaou, R. Zeller, and P. H. Dederichs, Phys. Rev. B **62**, 452 (2000).

[46]S. Cottenier and H. Haas, Phys. Rev. B **62**, 461 (2000).

[47]L. A. Errico, G. Fabricius, and M. Rentería, Phys. Status Solidi B **241**, 2394 (2004).

[48]R. Vidya, P. Ravindran, H. Fjellvåg, B. G. Svensson, E. Monakhov, M. Ganchenkova, and R. M. Nieminen, Phys. Rev. B **83**, 045206 (2011).

[49]G. Weyer, H. P. Gunnlaugsson, R. Mantovan, M. Fanciulli, D. Naidoo, K. Bharuth-Ram, and T. Agne, J. Appl. Phys. **102**, 113915 (2007).

[50]T. Mølholt, R. Mantovan, H. Gunnlaugsson, K. Bharuth-Ram, M. Fanciulli, H. Gíslason, K. Johnston, Y. Kobayashi, G. Langouche, H. Masenda, D. Naidoo, S. Ólafsson, R. Sielemann, and G. Weyer, Physica B **404**, 4820 (2009).

[51]H. P. Gunnlaugsson, T. E. Mølholt, R. Mantovan, H. Masenda, D. Naidoo, W. B. Dlamini, R. Sielemann, K. Bharuth-Ram, G. Weyer, K. Johnston, G. Langouche, S. Ólafsson, H. P. Gíslason, Y. Kobayashi, Y. Yoshida, and M. Fanciulli, Appl. Phys. Lett. **97**, 142501 (2010).

[52]R. Mantovan, H. P. Gunnlaugsson, D. Naidoo, S. Ólafsson, K. Johnston, H. Masenda, T. E. Mølholt, K. Bharuth-Ram, M. Fanciulli, H. P. Gislason, G. Langouche, R. Sielemann, and G. Weyer, and T. I. Collaboration, J. Phys. Condens. Matter **24**, 485801 (2012).

[53]T. E. Mølholt, H. P. Gunnlaugsson, K. Johnston, R. Mantovan, H. Masenda, D. Naidoo, S. Ólafsson, K. Bharuth-Ram, H. P. Gislason, G. Langouche, R. Sielemann, G. Weyer, and T. I. Collaboration, Phys. Scr. **T148**, 014006 (2012).

[54]A. Janotti and C. G. Van de Walle, Phys. Rev. B **76**, 165202 (2007).

[55]T. Kataoka, M. Kobayashi, Y. Sakamoto, G. S. Song, A. Fujimori, F.-H. Chang, H.-J. Lin, D. J. Huang, C. T. Chen, T. Ohkochi, Y. Takeda, T. Okane, Y. Saitoh, H. Yamagami, A. Tanaka, S. K. Mandal, T. K. Nath, D. Karmakar, and I. Dasgupta, J. Appl. Phys. **107**, 033718 (2010).

[56]Y. Abreu, C. Cruz, I. Piñera, A. Leyva, A. Cabal, and P. V. Espen, Solid State Commun. **185**, 25 (2014).

[57]C. Schäfer, W. Potzel, W. Adlassnig, P. Pöttig, E. Ikonen, and G. M. Kalvius, Phys. Rev. B **37**, 7247 (1988).

[58]N. S. Laulainen and M. N. McDermott, Phys. Rev. **177**, 1606 (1969).